ACS APPLIED MATERIALS & INTERFACES

www.acsami.org

Research Article

Exotic Quad-Domain Textures and Transport Characteristics of Self-Assembled $BiFeO_3$ Nanoislands on Nb-Doped $SrTiO_3$

Lili Ding, Ye Ji, Xiaoyue Zhang, Mengjun Wu, Yue Zheng, Biao Wang,* and Weijin Chen*

Cite This: *ACS Appl. Mater. Interfaces* 2021, 13, 12331−12340

Read Online

ACCESS | Metrics & More | Article Recommendations | Supporting Information

ABSTRACT: Topological quad-domain textures with interesting cross-shaped buffer domains (walls) have been recently observed in $BiFeO_3$ (BFO) nanoislands, indicating a new platform for exploring topological defects and multilevel memories. Such domain textures have nevertheless only been limited in BFO nanoislands grown on $LaAlO_3$ substrates with a large lattice mismatch of ∼−4.4%. Here, we report that such exotic domain textures could also form in BFO nanoislands directly grown on a conductive substrate with a much smaller lattice mismatch and the local transport characteristics of the BFO nanoislands are distinct from the previously reported ones. The angle-resolved piezoresponse force images verify that the domain textures consist of center-divergent quad-domains with upward polarizations and cross-shaped buffer domains with downward polarizations. Interestingly, textures with multiple crosses are also observed in nanoislands of larger sizes, besides the previously reported ones with a single cross. The nanoislands exhibit strong diodelike rectifying characteristics and the quad-domains show a higher average conductance than the cross-shaped buffer domains, indicating that there is a certain correlation between the local conductance of the nanoislands and the domain textures. This transport behavior is attributed to the effect of the depolarization field on the Schottky barriers at both the substrate/BFO interface and the tip/BFO junction. Our findings extend the current understanding of the exotic quad-domain textures of ferroelectric nanoislands and shed light on their potential applications for configurable electronic devices.

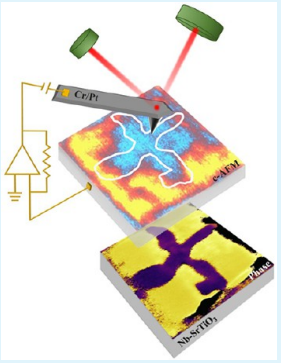

KEYWORDS: *ferroelectric, BFO, nanoisland, topological defects, PFM, conductance*

1. INTRODUCTION

Exotic polarization textures with nontrivial topological features, *e.g.*, flux-closing or center-type vortices, skyrmions, *etc.*, have been observed in ferroelectrics when the system dimensions are at nanoscale.[1−5] These polarization textures are fundamentally important and technologically attractive for their novel physical properties and useful concepts of new electronic devices.[6−9] For example, polar vortices can be stabilized in quite small sizes (<10 nm), suggesting the potential to increase the storage density of ferroelectric memories over Tb/inch^2.[1] The fascinating properties of polar vortices like the novel phase transformation paths under electrical and mechanical stimuli,[10−16] the high electronic conductance,[17,18] the high negative capacitance near the vortex core,[19,20] *etc.*, also hold promise for the design of innovative configurable electronic devices.

More recently, novel center-type quadrant domain textures with vortice defects have been reported in epitaxial $BiFeO_3$ (BFO) square nanoislands grown on $LaAlO_3$ (LAO) substrates.[21−26] These domain textures consist of four quad-domains separated either by cross-shaped domain walls[21−24] or buffer domains,[25,26] which hereafter we would like to call type-I and type-II textures, respectively. While looking similar in piezoresponse force microscopy (PFM), these two domain textures are actually different as revealed by previous works. Specifically, for type-I texture, the quad-domains are spontaneous center-convergent (with low-conducting and head-to-head domain walls) and can be switched to be center-divergent (with high-conducting and tail-to-tail domain walls), implying a good candidate for domain-wall electronic devices.[21] Phase-field modeling attributed the formation of this domain texture to the combining effects of geometrical constraint, electric boundary condition, and mobile charges.[22] For type-II texture, the as-grown state consists of center-divergent quad-domains with upward polarizations and cross-shaped buffer domains with inward/downward polarizations.[25,26] The buffer domains can be delicately controlled *via* a nonlocal way by electrical switching of the quad-domains, accompanied by the pair creation and annihilation of vortices and antivortices. Interestingly, enhanced electronic conduction occurs near the side walls of the as-grown nanoislands in type-II texture (with the $Pr_{0.5}Ca_{0.5}MnO_3$ layer as a bottom electrode) and the enhanced electronic conduction is suppressed by 180° polarization switching in a reversible way.[26] Different from type-I texture, the formation of the type-II texture is considered to be caused by the strong shear-strain−

Received: November 3, 2020
Accepted: February 19, 2021
Published: March 4, 2021

polarization coupling and the flexoelectric effect associated with strain gradients due to a relaxation of the misfit strain between $LaAlO_3$ substrates and BFO. Despite these interesting findings, so far center-type quadrant domain textures have only been observed in BFO nanoislands on $LaAlO_3$ substrates with a large lattice mismatch ∼−4.4%. It is of practical significance to ask if such domain textures could also form in BFO nanoislands on other substrates particularly those with a smaller lattice mismatch. Moreover, how the local electron transport properties of BFO nanoislands with such domain textures would be modified by the substrate/BFO interface environment is far from clear.

In this work, we report successful growth of self-assembled BFO nanoislands with type-II-like domain textures on a conductive 0.5% Nb-doped (001) $SrTiO_3$ (STO) substrate *via* a pulsed laser deposition (PLD) method. The lattice mismatch between the BFO and STO is ∼−1.5%, which is much smaller than that between BFO and LAO. The detailed intrastructure and the local transport characteristics of the exotic domain textures were characterized *via* angle-resolved piezoresponse force microscopy (PFM) and conductive atomic force microscopy (c-AFM), respectively. Interestingly, besides the previously reported textures with a single cross, textures with multiple crosses are also observed in nanoislands with a larger size. Due to the Schottky barriers at both the substrate/BFO interface and the tip/BFO junction, overall diodelike rectifying characteristics is observed in the nanoislands. Moreover, the quad-domains exhibit a higher average conductance than the cross-shaped buffer domains, indicating that there is a certain correlation between the local conductance of the nanoislands and the domain textures. A feasible manipulation of the domain textures *via* the PFM tip field is also examined. A phase-field simulation was also presented to help better understand the formation of such exotic domain textures in BFO nanoislands.

2. EXPERIMENTAL SECTION

2.1. Growth of BFO Nanoislands. As schematically illustrated in Figure 1, the BFO nanoislands were grown on a 0.5% Nb-doped (001) STO substrate *via* a template-free PLD method. Before deposition, the substrate was first cleaned by acetone, isopropyl alcohol, ethanol, and deionized water *via* ultrasound. A KrF excimer laser (λ = 248 nm) was employed as the pulsed laser source focusing on the rotating BFO target with a laser energy of 300 mJ and a pulse frequency of 5 Hz. During deposition, the substrate was heated at 600 °C and an oxygen partial pressure of 20 Pa. After 5000 laser pulse deposition, the sample was annealed at 650 °C and oxygen partial pressure of 5 kPa for 10 min. The sample was cooled down to 300 °C at a cooling rate of 5 °C/min and then was cooled naturally to room temperature.

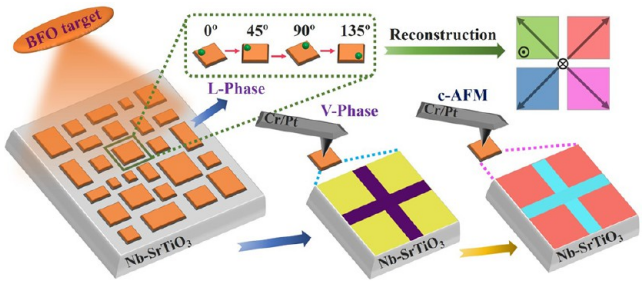

Figure 1. Schematic of the research framework of this study. BFO nanoislands were directly grown on a Nb-doped STO substrate by a template-free PLD method. To fully reveal the domain structure of the nanoislands, both vertical and lateral PFM mappings are performed. An angle-resolved PFM technique was adopted with four lateral PFM phase images acquired in a quasi-identical region at different sample orientations. c-AFM measurement was then applied to obtain the local current−voltage curves and the current maps of the nanoislands.

2.2. Structure and Morphology Analysis. Structural characterization of the sample was carried out *via* a Rigaku X-ray diffraction (XRD) system with Cu Kα radiation (wavelength λ = 1.5405 Å) at a working voltage of 40 kV and a working current of 36 mA. The morphology of the BFO nanoislands was revealed by a Quanta FEG scanning electron microscope (SEM) and the atomic force microscope (AFM) mode of an Asylum Research MFP-3D scanning probe microscope (SPM).

2.3. PFM and c-AFM Analyses. The local piezoresponse loops and the piezoresponse vector maps of the BFO nanoislands are obtained by PFM (MFP-3D SPM). The local current−voltage curves and the current maps of the nanoislands were tested by c-AFM (MFP-3D SPM), with a Femto DLPCA-200 current amplifier integrated into the AFM circuit. A dual-frequency resonance-tracking technique was adopted to improve the PFM sensitivity. In construction of the domain structures of the BFO nanoislands, an angle-resolved PFM technique was adopted with four lateral PFM images acquired in a quasi-identical region at different sample orientation angles, as shown in Figure 1. In the electrical writing and erasing of the domain textures *via* a PFM tip, we used a high voltage holder to ensure that the nanoislands were subjected to a large enough voltage variation range. Cr−Pt-coated conducting tips (Budget sensors) were acting as the top electrode in all of the AFM, PFM, and c-AFM measurements.

2.4. Phase-Field Simulation. In the phase-field simulation, both the polarization $\mathbf{P} = (P_1, P_2, P_3)$ and oxygen octahedral tilt order parameter $\boldsymbol{\theta} = (\theta_1, \theta_2, \theta_3)$ are introduced to describe the domain structure of the BFO nanoislands.[25−27] The total free energy of the system includes the contributions from the Landau bulk free energy, gradient energy, elastic energy, electrostatic energy, surface energy, and flexoelectric energy. To account for the effect of substrate clamping, the BFO nanoisland is modeled with an eigenstrain caused by lattice parameter mismatch between BFO and the substrate, and the displacement is fixed to be zero at the bottom surface of the nanoisland. Finite element methods (FEMs) are adopted to solve the electric field and mechanical strain and stress fields according to the electrostatic and mechanical equilibrium equations, respectively. The evolution of polarization and oxygen octahedral tilt order parameter is captured by corresponding time-dependent Ginzburg−Landau (TDGL) equations, which are numerically solved *via* the Euler iteration method. The BFO nanoisland is discretized by a grid of $48\Delta x \times 48\Delta x \times 10\Delta x$ with Δx = 0.4 nm.

3. RESULTS AND DISCUSSION

3.1. Quad-Domain Textures of the BFO Nanoislands. The XRD diffractogram of the as-grown BFO nanoisland sample is shown in Figure 2a. The XRD spectra exhibit clear feature peaks at (001) and (002) orientations of BFO and the STO substrate, which indicates a high crystalline quality of the BFO nanoislands. The good-quality growth of the nanoislands is also confirmed from the SEM images (Figure S1). It is clear that the nanoislands are in a quadrilateral shape but with different lateral sizes ranging from 50 to 500 nm. The thicknesses of the nanoislands are about 20 nm as inferred from the scale of the AFM topography image shown in Figure 2c. Note, from the thermodynamic point of view, that for the growth of self-assembled BFO nanoislands, three-dimensional (3D) island growth mode is less favored for STO substrates compared with LAO substrates due to the much less misfit strain. The growth of our nanoislands is likely to be determined by kinetics rather than by thermodynamics (see

https://dx.doi.org/10.1021/acsami.0c19652
ACS Appl. Mater. Interfaces 2021, 13, 12331−12340

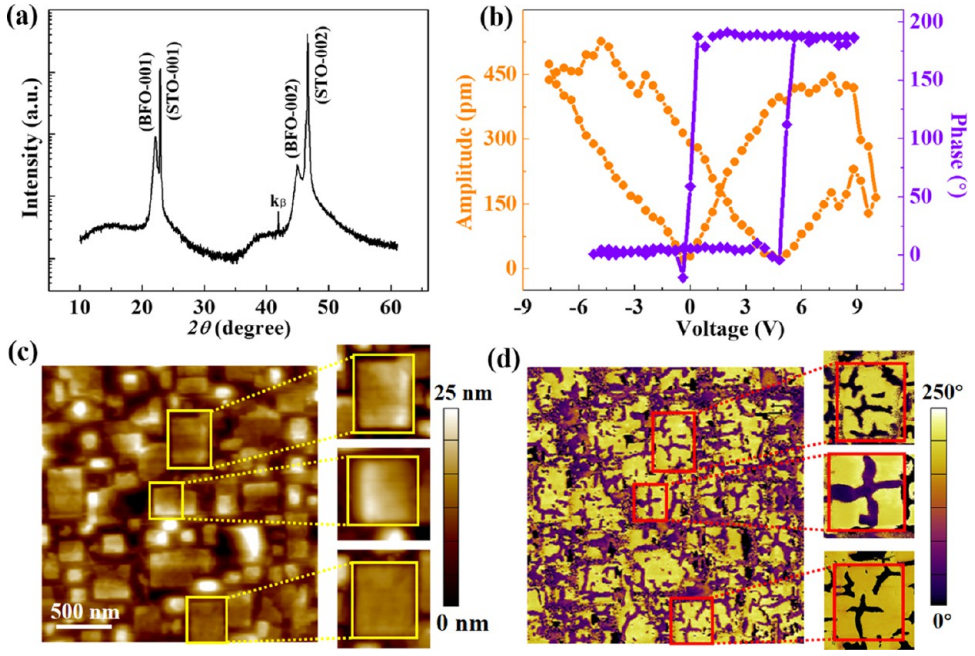

Figure 2. (a) XRD diffractogram of the nanoislands sample. (b) PFM phase−voltage hysteresis loop and butterfly-like amplitude−voltage loop at a selected nanoisland. (c) AFM topography image of a selected area (2.4 μm × 2.4 μm) and the enlarged AFM images nearby three selected nanoislands. (d) Vertical phase (V-phase) PFM mapping of a selected area and the enlarged V-phase images nearby three selected nanoislands. The scanning area is the same as (c).

more discussion in the Supporting Information). The piezoresponse phase and amplitude as functions of PFM tip bias at a selected point of the nanoisland region are measured and shown in Figure 2b. The clear hysteresis loops of the PFM phase and amplitude indicate a good ferroelectric characteristic of the nanoislands. A shift of the hysteresis loop of about ∼2 V along the positive voltage axis is also seen, suggesting that the BFO nanoislands are subjected to an upward built-in field of ∼1 MV/cm if we take the thickness of the nanoisland to be 20 nm. Such an upward built-in field can be mainly correlated to the Schottky diodes formed at the interfaces between BFO and the Nb-STO substrate and that between BFO and the PFM tip. According to the values of the work functions of the three materials (W_{Pt} = 5.36 eV, W_{BFO} = 4.7 eV, and W_{STO} = 4.08 eV),[28,29] we can estimate a built-in voltage of about 1.3 V (W_{Pt} − W_{STO}). The value is smaller than the experimental value (∼2 V), and the difference can be attributed to the upward flexoelectric field caused by the relaxation of the lattice misfit strain.

A typical vertical phase (V-phase) PFM mapping of the nanoislands is shown in Figure 2d. The corresponding vertical amplitude PFM image is shown in Figure S2. The scanning area (2.4 μm × 2.4 μm) is the same as that in Figure 2c. The sample shows a clear phase contrast and a dominant polarization direction (upward, yellow color), implying the existence of an upward built-in field. Note, the PFM amplitude is quite small in the off-island regions, as shown in Figure S2, indicating that there is no BFO in the gap regions and the self-assembled nanoislands are isolated. This is in contrast to those embedded in a T-phase BFO film or a $CeFe_2O_4$ film for BFO nanoislands grown on $LaAlO_3$ substrates.[21−26] Moreover, the nanoislands exhibit a tendency of forming type-II-like cross-shaped domain textures, similar to those grown on $LaAlO_3$.[21−26] To see clearly, three nanoislands were further picked out to carry PFM mapping within a smaller area. The obtained enlarged V-phase images of these three nanoislands are depicted in Figure 2d. The corresponding vertical amplitude PFM images are shown in Figure S3. One can see that cross-shaped domain textures can indeed be stabilized in BFO nanoislands grown on the Nb-STO substrate, which brings a much smaller lattice mismatch (∼−1.5%) than that of the $LaAlO_3$ substrate (∼−4.4%). It is worth noting that besides the domain textures with a single cross of buffer domains as reported in previous works, domain textures with multiple crosses of buffer domains are observed in nanoislands with larger sizes, verifying an interesting size effect. The mechanism of such a size effect is not clear and may be caused by the disturbance of the clamping strain relaxation by the imperfections (*e.g.*, grain boundaries and dislocations) of the nanoislands.

To investigate the cross-shaped domain textures of the nanoislands in detail, we further performed a vector PFM measurement *via* an angle-resolved technique.[25,30] In the measurement, the nanoisland sample was rotated at four orientations (*i.e.*, 0, 45, 90, and 135°) in the in-plane direction. Then, PFM in a dual ac resonance track mode was used to measure the vertical and lateral piezoresponse signals in a quasi-identical region for each sample orientation. In Figure 3a−c, the surface topography, lateral PFM phase (L-phase), and amplitude images of a square nanoisland (the size of which is about 250 nm × 250 nm) at four orientations are depicted, respectively. Note that the V-phase image of the nanoisland is shown in Figure 2d. From the topography image, the nanoisland has a quite flat surface and sharp edges, implying good crystallinity. The formation of a cross-shaped domain texture with a single cross is indicated both by the L-phase and amplitude images. One can also note that the cross-shaped buffer domains show a generally weaker piezoresponse than the quad-domains. The angle-dependences of the lateral phase and amplitude of the quad-domains are clearly seen.

https://dx.doi.org/10.1021/acsami.0c19652
ACS Appl. Mater. Interfaces 2021, 13, 12331−12340

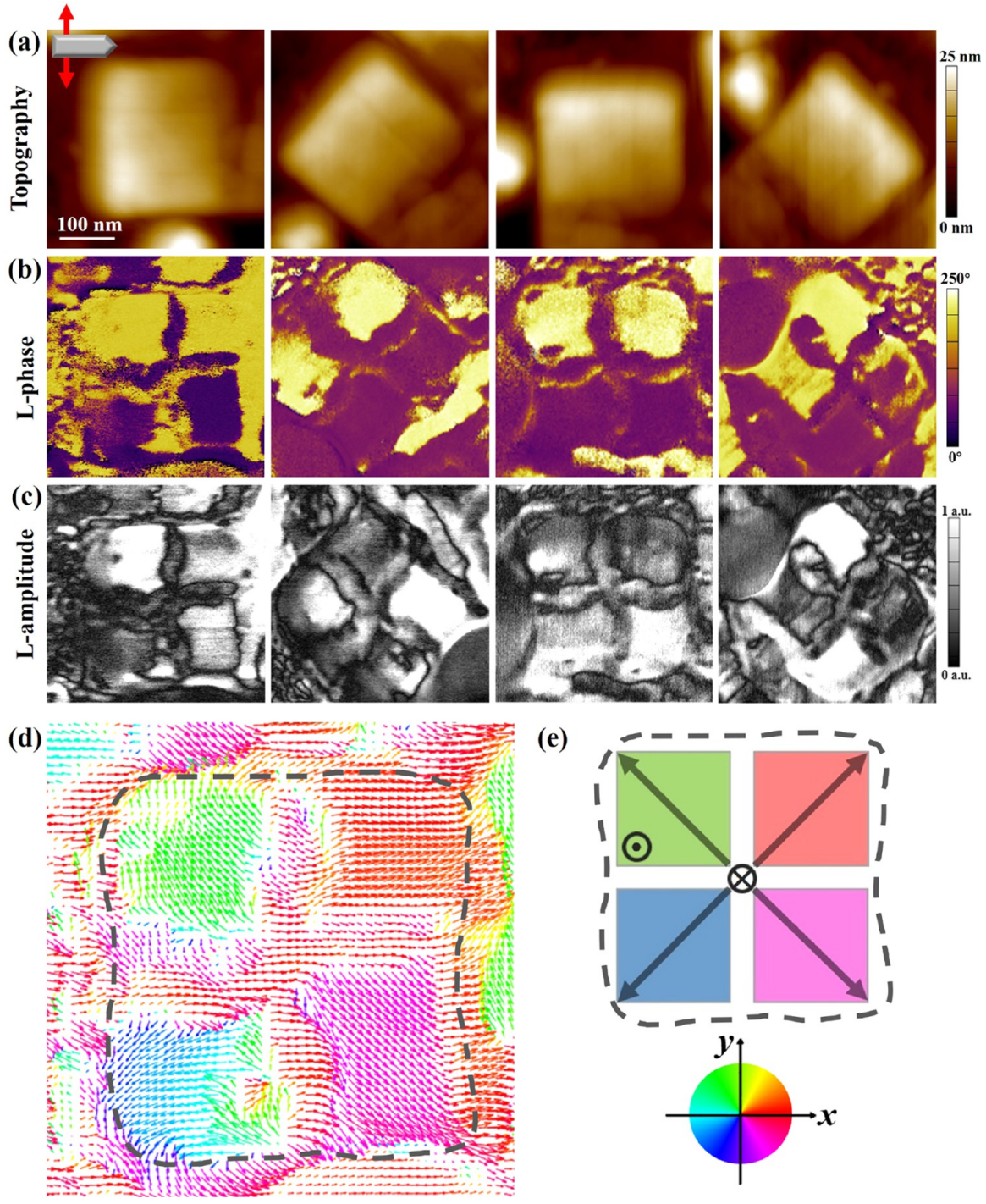

Figure 3. (a–c) Surface topography, lateral PFM phase, and amplitude images of a square nanoisland at four sample orientation angles (*i.e.*, 0, 45, 90, and 135°). The orientation of the tip is fixed in the measurement as indicated in (a). (d) Reconstructed in-plane polarization distribution of the nanoisland. (e) Simplified diagram of the domain texture. The color map of the in-plane polarization direction for the plot of (d) is also shown in (e).

Based on the lateral PFM phase (L-phase) and amplitude data at four orientations, we then reconstructed in-plane polarization distribution of the nanoisland, as shown in Figure 3d. Details of the polarization reconstruction procedures are described in the Supporting Information. A simplified diagram of the domain texture is also shown in Figure 3e. From the reconstructed polarization field, one can see that the nanoisland forms a type-II-like domain texture quite similar to that reported in BFO nanoislands grown on $LaAlO_3$ substrates.[25,26] The domain texture consists of center-divergent quad-domains with upward polarizations and cross-shaped buffer domains with downward polarizations. Possible driving forces of the forming of this exotic domain texture are (a) the shear strains, (b) the flexoelectric field, and (c) the depolarization/built-in fields, as suggested by previous works.[25,26] Our phase-field simulation (see the Supporting Information) demonstrates that the BFO nanoisland can evolve into a type-II domain texture without an a priori

https://dx.doi.org/10.1021/acsami.0c19652
ACS Appl. Mater. Interfaces 2021, 13, 12331–12340

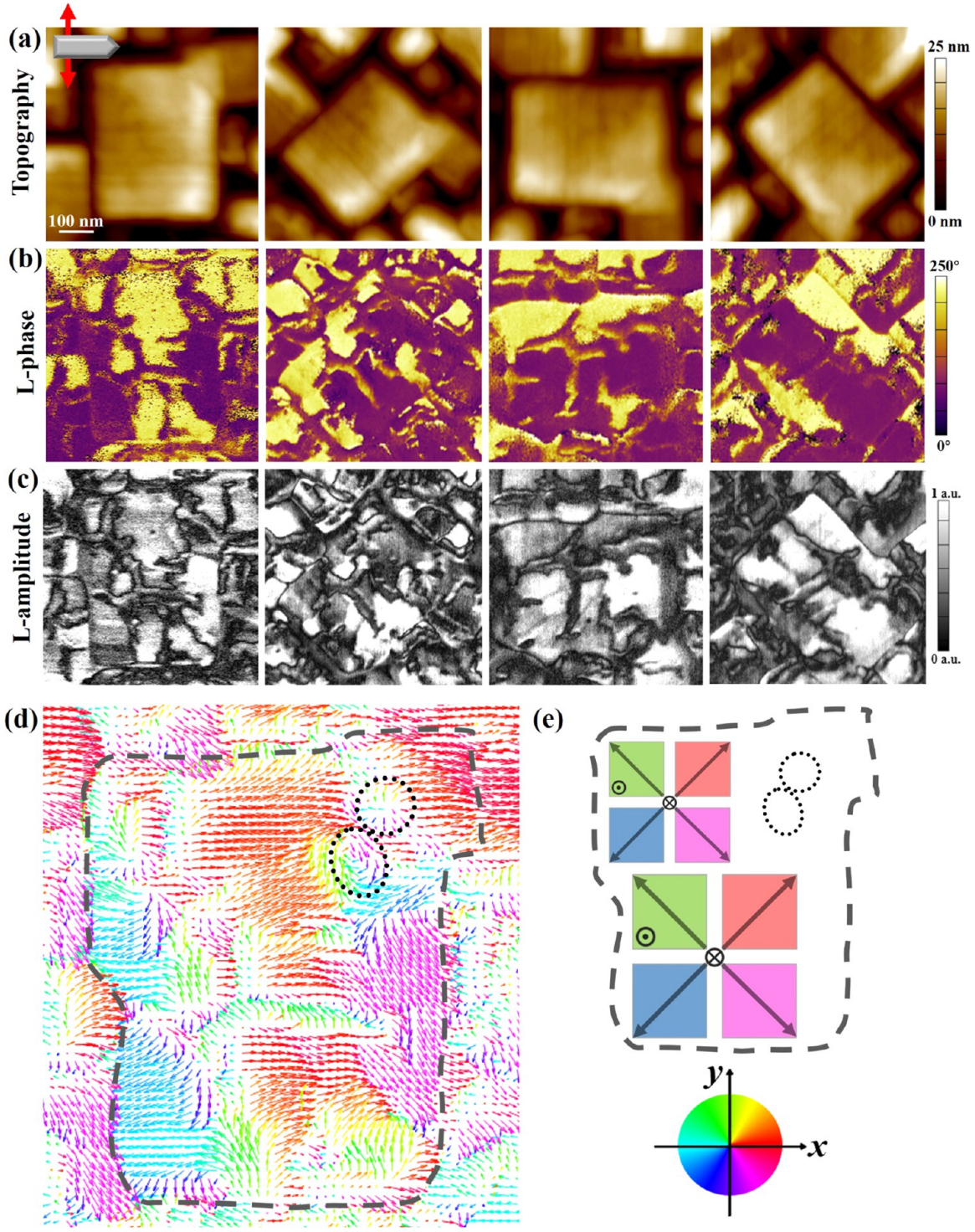

Figure 4. (a–c) Surface topography, lateral PFM phase, and amplitude images of a rectangular nanoisland at four sample orientation angles (*i.e.*, 0, 45, 90, and 135°). The orientation of tip is indicated in (a). (d) Reconstructed in-plane polarization distribution of the nanoisland. (e) Simplified diagram of the domain texture. The color map of the in-plane polarization direction for the plot of (d) is also shown in (e). The two dot circles in (d) and (e) indicate a flux-closure vortex and a center-divergent vortex, respectively.

assumption of the polarization distribution and without the necessity to artificially adjust the strengths of the flexoelectric and electrostatic fields. Specifically, due to a relaxation of the misfit strain between the Nb-STO substrate and the BFO nanoisland, large shear strains are induced in the nanoisland and they show alternating signs at the four quadrants of the nanoisland (Figure S6). To minimize the coupling energy between shear strains and polarization, the polarization vector of the rhombohedral BFO has to be either inward (when the out-of-plane component $P_z < 0$) or outward (when $P_z > 0$) at each quadrant. Meanwhile, due to the strain gradients, an outward/upward flexoelectric field would arise. An upward built-in field would also arise due to the formation of a Schottky barrier at the Nb-STO/BFO interface. Both fields

https://dx.doi.org/10.1021/acsami.0c19652
ACS Appl. Mater. Interfaces 2021, 13, 12331−12340

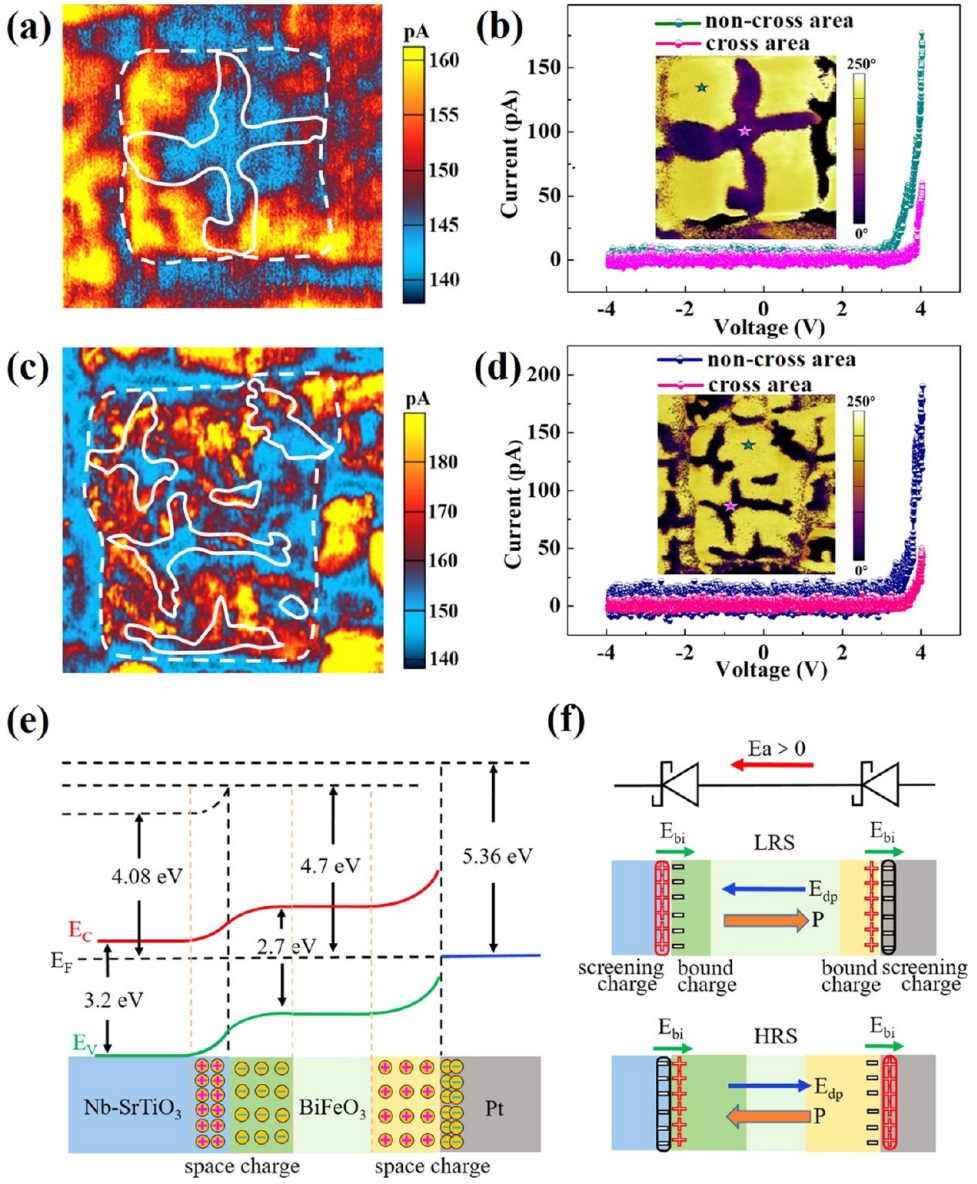

Figure 5. Local transport characteristics of two selected BFO nanoislands measured by c-AFM. The c-AFM mapping images under a tip bias of +4 V of (a) square nanoisland and (c) rectangular nanoisland. White solid lines are the boundaries of the cross-shaped buffer domains obtained from the PFM V-phase images. (b–d) Local current–voltage curves at points located at the quad-domains and the cross-shaped buffer domains of the two nanoislands. The selected points are marked by the stars in the inserted PFM V-phase images of the nanoislands. (e) Schematic energy band of the Nb-STO/BFO/Pt heterostructure. (f) Illustration of the polarization effect on the conductance of the heterostructure, with upward polarization state (upper panel) and downward polarization state (bottom panel) corresponding to the low resistance state (LRS) and high resistance state (HRS), respectively.

favor an upward polarization in the quad-domains and hence stabilize the center-divergent quad-domains. Moreover, cross-shaped buffer domains instead of tail-to-tail charge domain walls are formed to reduce both the electrostatic and elastic energies. Note, oxygen vacancies may play a role in the formation of the quad-domain texture of the BFO nanoislands, especially in the stabilization of type-I quad-domain textures with head-to-head charge domain walls,[21,22] as they can provide free electrons to screen head-to-head charged domain walls. Their nonuniform distribution can also modify the strain gradients of the nanoislands and hence affect the flexoelectric field. Nevertheless, our nanoislands were grown at an oxygen pressure of 20 Pa and were annealed at an oxygen pressure of 5 kPa. The relatively large oxygen pressures during the deposition and annealing processes provide the condition for the nanoislands to be sufficiently oxygenated with few oxygen vacancies. Therefore, we do not expect that the oxygen vacancies would play an important role in the formation of the quad-domain structure. On the other hand, as shown in the following, some of our nanoislands do exhibit some head-to-head charged domain walls, implying a possible role of oxygen vacancies. Anyway, due to the uncertainty of the concentration of oxygen vacancies, it is hard to exclude the effect of oxygen vacancies on the quad-domain textures.

We further performed the vector PFM measurement on a rectangular nanoisland, which forms a domain texture with more than one cross, as indicated by the V-phase image shown in Figure 2d. The size of the nanoisland is about 350 nm × 450

https://dx.doi.org/10.1021/acsami.0c19652
ACS Appl. Mater. Interfaces 2021, 13, 12331–12340

nm. The surface topography, lateral PFM phase, and amplitude images of the nanoisland at four lateral orientations (*i.e.*, 0, 45, 90, and 135°) are shown in Figure 4a−c, respectively. The obtained lateral PFM phase and amplitude images of the nanoisland are much complicated than those of the previously studied one shown in Figure 3. Nevertheless, the cross-shaped texture can still be easily seen. From the reconstructed lateral polarization distribution of the nanoisland in Figure 4d, one can identify two cross-shaped buffer domain regions in the nanoisland, and each of the cross-shaped buffer domain regions is surrounded by four center-divergent quad-domains. To see this more clearly, a simplified diagram of the domain texture is also shown in Figure 4e. The formation of such a domain texture with multiple-cross-shaped regions may be caused by the disturbance of the clamping strain relaxation by the imperfections (*e.g.*, grain boundaries and dislocations) of the nanoislands. It is also worth noting that a flux-closure vortex and a center-divergent vortex (see the dot circles in Figure 4d,e) are also found in the upper right region of the nanoisland. The coexistence of the cross-shaped domain texture and the topological defects indicates the complexity of the domain texture.

Note also that the detailed intrastructures of cross-shaped buffer domains are not the same for the two BFO nanoislands, as shown in Figures 3d and 4d. Such in-plane textures of the buffer domains are also different from those in nanoislands on LAO substrates reported in previous works,[25,26] though the overall domain textures look quite similar. As shown by phase-field simulation and thermodynamic analysis,[25] BFO nanoislands can stabilize various configurations of cross-shaped buffer domains. To mostly reduce both the electrostatic energy and the elastic energy of the nanoisland with quad-domains, each buffer domain tends to form a 109° ferroelastic domain wall and a 180° ferroelectric domain wall with the two adjacent quad-domains since these domain walls possess lower domain wall energies compared with the 71° ferroelastic domain walls (with optimized oxygen octahedral tilts).[27] For our BFO nanoislands, the constructed polarization distributions of the buffer domains do not overall match with the above scenario. For the square nanoisland (Figure 3d), a buffer domain with downward/outward polarization rather than downward/inward polarization is formed between the first and fourth quad-domains. For the rectangular nanoisland (Figure 4d), head-to-head charge walls are observed in the buffer domain region. Such differences indicate that the realistic conditions of our nanoislands are more complicated than those assumed in the theoretical model. However, we must be aware that there are probably some artificial defects of the constructed polarization map caused by the nonideality of the PFM imaging and angle-resolved technique. The constructed polarization map in the buffer domain regions is not as reliable as that in the quad-domain regions.

3.2. Transport Characteristics of the BFO Nanoislands. Note, in our system, Nb-STO acts as not only a substrate but also a bottom electrode. This is in contrast with previous systems where (La,Sr)MnO_3 or $Pr_{0.5}Ca_{0.5}MnO_3$ layers were deposited on $LaAlO_3$ as the bottom electrodes.[21−26] As the Nb-STO/BFO interface is quite different from those in the previous systems, the transport properties of the quad-domain textures should be distinct. The next important issue is thus how the local transport characteristics of the BFO nanoislands are affected by the quad-domain textures and the Nb-STO/BFO interface environment. As the BFO nanoislands were directly grown on a conductive Nb-STO substrate and Cr−Pt tips were adopted in the c-AFM measurement, a strong forward diode behavior is expected due to the formation of Schottky barriers at the Nb-STO/BFO and BFO/tip interfaces. For comparison, the conductivity of the bare Nb-doped STO substrate was first measured by c-AFM, and the measured current of the bare substrate is on the order of nanoampere (Figure S8). Note that this current value is an order of magnitude higher than that measured at the BFO nanoislands, verifying that the c-AFM measurement can reveal the true conductance of the BFO nanoislands. The c-AFM mapping images under a tip bias of +4 V of the two selected BFO nanoislands are depicted in Figure 5a,c, respectively. Their domain textures were previously reconstructed in the last section. To better see the correlation of the conductance with the domain texture, we also mark the boundaries of the buffer domains on the c-AFM images, and the histograms of current distribution at the buffer domains region (*i.e.*, with downward polarization) and the nonbuffer domain region (*i.e.*, with upward polarization) of the nanoislands are plotted and shown in Figure S9. From the c-AFM images and histograms of current distribution, one can see that for both nanoislands, the buffer domains possess a lower average conductance than the nonbuffer domains. While the area of buffer domains is much smaller than that of the nonbuffer domains, the buffer domains show relatively more pixels at small currents. Meanwhile, there is also an obvious mismatch between the c-AFM and the PFM images, leading to similar current ranges of the buffer domains and the nonbuffer domains. Our result therefore shows that there is a certain correlation between the local conductance and the domain texture of the nanoislands, but there are also strong nonlocal effects.

We further measured the local current−voltage curves at selected points located at the quad-domains and the cross-shaped buffer domains of the two nanoislands, as shown in Figure 5b,d. The selected points are marked by the green and pink stars in the inserted PFM V-phase images of the two nanoislands. From the current−voltage curves, both nanoislands exhibit an overall Schottky diode behavior with a forward direction under a positive tip voltage as expected. Moreover, the quad-domains of both nanoislands exhibit higher forward conduction currents than the cross-shaped buffer domains. At the tip bias of +4 V, the local current values at the quad-domains are about four times those at the cross-shaped buffer domains. This is consistent with the c-AFM mapping results and indicates a strong effect of the polarization state on the local transport property of the nanoislands.

Note that the transport characteristics of our BFO nanoislands are quite different from the previously reported BFO nanoislands in type-II textures (with a bottom electrode $Pr_{0.5}Ca_{0.5}MnO_3$ layer and surrounded by $CoFe_2O_4$ clusters),[26] where enhanced conduction near the side walls of the nanoislands was observed and was attributed to the band bending near the side interfaces between BFO and $CoFe_2O_4$. For our sample, there are no side interfacial junctions, and a certain correspondence between the local domain texture and the conductance is observed. The buffer domains with downward polarization possess a lower average conductance than the nonbuffer domains with upward polarization. Several possible sources can cause the mismatch of the c-AFM mapping and the PFM mapping. The first is the nonlocal effect of the polarization field on the distributions of free charge carriers and electrostatic potential due to the long-range

https://dx.doi.org/10.1021/acsami.0c19652
ACS Appl. Mater. Interfaces 2021, 13, 12331−12340

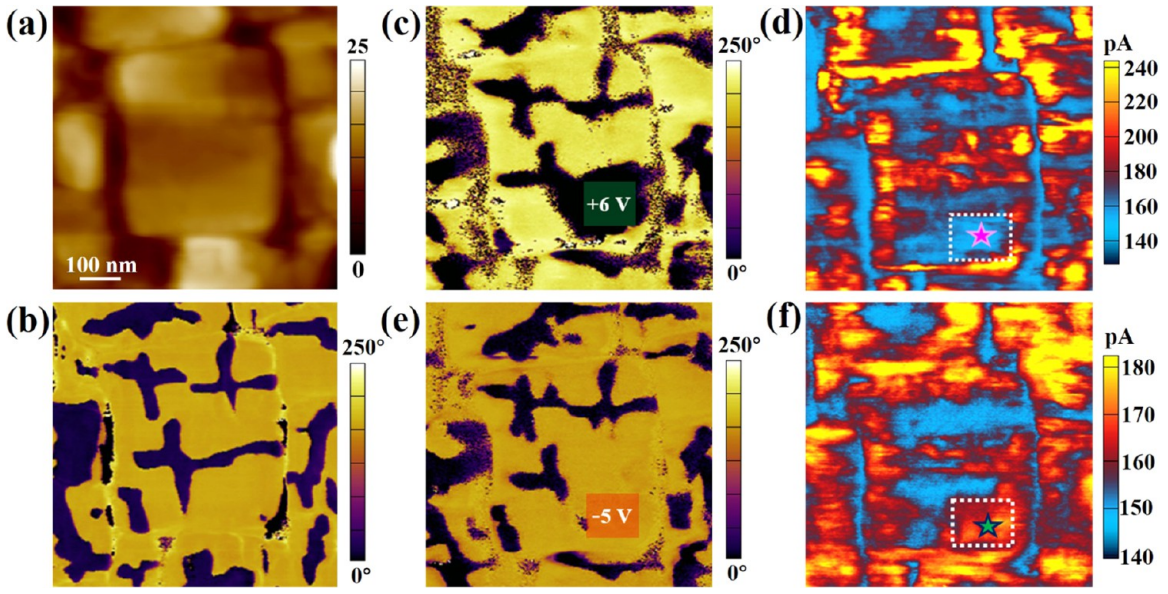

Figure 6. Evolution of the domain texture and the local conductance of a rectangular nanoisland with a multiple-cross-shaped domain texture after first applying a tip bias of +6 V and then −5 V at the right bottom quad-domain region of the nanoisland. (a) AFM topography and (b) PFM V-phase image of the nanoisland before applying a tip bias. (c) PFM V-phase and (d) c-AFM images of the nanoisland after applying a tip bias of +6 V at the right bottom quad-domain. (e) PFM V-phase and (f) c-AFM images of the nanoisland after applying a tip bias of −5 V at the same region.

electrostatic interaction and the limited amount of free charge carriers. The second is the spatial inhomogeneity of Nb-STO substrate conductance, as shown in Figure S8. The third is the side-wall effect, which tends to increase the contact area between the tip and the nanoisland and hence increase the c-AFM current near the side walls of the nanoisland. Moreover, the c-AFM resolution and repeatability are limited by unfavored factors like the tip wear problem and the instrument noise.

The charge environments at the interfaces, which are affected by both the work functions of materials and the polarization states, should play important roles in the observed transport characteristics of the BFO nanoislands. The overall Schottky diode behavior of the nanoislands can be related to the forward Schottky barriers formed at both the Nb-STO/BFO and the BFO/tip interfaces.[28,29] Nevertheless, the observed low resistance state (LRS) of the upward quad-domains and the high resistance state (HRS) of the downward cross-shaped buffer domains are against the mechanism reported in previous works,[28,29] which show that BFO films or nanoislands in upward polarization are in HRS due to the increase of the width of depletion region by the polarization. What is worth noting is that previously reported BFO nanoislands with type-II textures on $LaAlO_3$ substrates also exhibited a decrease of conductance when the whole texture was switched to a downward domain texture.[26] A possible explanation of the unusual transport behavior of our BFO nanoislands might be as follows. A schematic energy band of the heterostructure is shown in Figure 5e, and the polarization effect on the conductance is illustrated in Figure 5f. The Schottky barriers at Nb-STO/BFO and the BFO/tip interfaces have positive built-in fields and are in a forward direction at a positive tip bias ($E_a > 0$). When the polarization is upward as in the quad-domains, a negative depolarization field appears and acts like the role of positive tip bias, which narrows the depletion layers and causes a low resistance state. For the case of downward polarization as in the region of cross-shaped buffer domains, the role of the depolarization field reverses and leads to an increase of the depletion width and the high resistance state.

A remaining issue is to demonstrate the controllability of the exotic cross-shaped domain texture and its local transport characteristics of the BFO nanoislands. Shown in Figure 6 are the PFM V-phase and c-AFM images of a rectangular nanoisland with a multiple-cross-shaped domain texture after first applying a tip bias of +6 V and then −5 V at the right bottom quad-domain of the nanoisland. As shown in Figure 6c, the initial upward quad-domain after applying +6 V tip bias was switched to downward and merged with the adjacent cross-shaped buffer domain. Meanwhile, a switching of the conductance from low resistance to high resistance occurs as shown by the c-AFM mapping image measured at a tip bias of +4 V (Figure 6d). After applying −5 V tip bias to the same area of the nanoisland (Figure 6e,f), the polarizations in this area were switched back to upward (with one arm of the cross-shaped buffer domains disappeared), accompanied by a recovery of low resistance. The reversible change of conductance is also clearly reflected by the local current−voltage curves of a selected point in the affected region (Figure S10). Note, applying a tip field can also cause interesting extension and regression of cross-shaped buffer domains of the BFO nanoislands, as shown in Figure S11, where a new buffer domain was generated like a tree branch extending from the intersection of two cross-shaped buffer domains. These results verify the facile controllability of the cross-shaped domain texture of the BFO nanoislands and hold promise for developing configurable electronic devices.

4. CONCLUSIONS

In summary, we used the pulsed laser deposition method to grow BFO nanoislands directly on a conductive Nb-doped STO substrate with a lattice mismatch of ∼−1.5%. We demonstrate that BFO nanoislands can still form intriguing quad-domain textures even under much smaller strain

https://dx.doi.org/10.1021/acsami.0c19652
ACS Appl. Mater. Interfaces 2021, 13, 12331−12340

gradients and flexoelectric field, compared with those grown on insulating $LaAlO_3$ substrates with a lattice mismatch of ~−4.4% as reported in previous works. Moreover, the transport characteristics of the BFO nanoislands are distinct from the previous systems, as revealed by angle-resolved piezoresponse force microscopy (PFM) and conductive atomic force microscopy (c-AFM). Besides the domain textures with a single cross of buffer domains as reported in previous works, domain textures with multiple crosses of buffer domains are commonly observed in nanoislands with larger sizes, verifying a size effect. Due to the Schottky barriers at both the substrate/BFO interface and the tip/BFO junction, an overall diode characteristic with a forward direction at positive tip bias is observed in the nanoislands. A certain correlation between the local conductance of the nanoislands and the domain textures is verified, with the quad-domains showing a higher average conductance than the cross-shaped buffer domains. A feasible manipulation of the domain textures *via* the PFM tip field is also examined. Our work extends the current understanding of exotic domain structures of ferroelectric nanoislands and demonstrates the potential of developing configurable electronic devices based on the exotic domain structures.

Note that the grown nanoislands are not uniform in size and are randomly distributed. This may limit its future applications as configurable electronic devices. A possible strategy to improve the size and distribution uniformity of PLD-deposited nanoislands is to use the template. Recently, a uniformly distributed $PbZr_{0.52}Ti_{0.48}O_3$ nanoisland array in the quadrilateral shape of unform size ~80 nm with the assistance of the anodic aluminum oxide (AAO) template has been successfully grown.[7] With the use of regular templates, it is promising to achieve a uniformly distributed BFO nanoisland array with quad-domain textures on the Nb-doped STO substrate. Moreover, other related oxides like $BaTiO_3$ and $Pb(Zr,Ti)O_3$ also have a rhombohedral phase at moderate misfit strain. They are candidate materials to explore similar quad-domain textures in a nanoisland structure. Other topological configurations such as flux-closure quadrants, vortices, and skyrmions are also possible to form under the combined effects of size, geometry, and electromechanical boundary conditions. Our recent work has shown that $PbZr_{0.52}Ti_{0.48}O_3$ nanoisland arrays on Nb-doped STO substrates can evolve into a center-divergent vortex pattern after applying a tip bias.[7] Such center-divergent pattern is similar to the quad-domain textures in BFO nanoislands. For future works, a transmission electron microscope (TEM) will be a powerful *in situ* tool to characterize and manipulate the quad-domain texture on the atomic scale. It is also interesting issues to explore the photoelectric and magnetic transport properties of the nanoislands *via* the combination of PFM, c-AFM, and the application of laser and magnetic fields.

■ ASSOCIATED CONTENT

Supporting Information

The Supporting Information is available free of charge at https://pubs.acs.org/doi/10.1021/acsami.0c19652.

Additional SEM/PFM images of the BFO nanoislands, reconstruction procedure of the polarization field in BFO nanoislands, phase-field simulation model and results, current−voltage characteristics of the bare Nb-STO substrate, histograms of c-AFM current distribution of the nanoislands, change of the current−voltage curve of a BFO nanoisland after applying a tip bias, and discussion on the growth mechanism of self-assembled BFO nanoislands (PDF)

■ AUTHOR INFORMATION

Corresponding Authors

Biao Wang − *School of Physics, Sun Yat-sen University, Guangzhou 510275, China*; Email: wangbiao@mail.sysu.edu.cn

Weijin Chen − *State Key Laboratory of Optoelectronic Materials and Technologies, School of Materials, Micro&Nano Physics and Mechanics Research Laboratory, School of Physics, and School of Physics, Sun Yat-sen University, Guangzhou 510275, China*; orcid.org/0000-0002-9276-7369; Email: chenweijin@mail.sysu.edu.cn

Authors

Lili Ding − *Micro&Nano Physics and Mechanics Research Laboratory, School of Physics and School of Physics, Sun Yat-sen University, Guangzhou 510275, China*

Ye Ji − *Micro&Nano Physics and Mechanics Research Laboratory, School of Physics and School of Physics, Sun Yat-sen University, Guangzhou 510275, China*

Xiaoyue Zhang − *Micro&Nano Physics and Mechanics Research Laboratory, School of Physics and School of Physics, Sun Yat-sen University, Guangzhou 510275, China*

Mengjun Wu − *Micro&Nano Physics and Mechanics Research Laboratory, School of Physics and School of Physics, Sun Yat-sen University, Guangzhou 510275, China*

Yue Zheng − *Micro&Nano Physics and Mechanics Research Laboratory, School of Physics and School of Physics, Sun Yat-sen University, Guangzhou 510275, China*; orcid.org/0000-0002-2165-7859

Complete contact information is available at: https://pubs.acs.org/10.1021/acsami.0c19652

Notes

The authors declare no competing financial interest.

■ ACKNOWLEDGMENTS

The authors acknowledge support from the NSFC (Nos. 11672339 and 11972382).

■ REFERENCES

(1) Naumov, I. I.; Bellaiche, L.; Fu, H. X. Unusual Phase Transitions in Ferroelectric Nanodisks and Nanorods. *Nature* **2004**, *432*, 737.

(2) Tang, Y. L.; Zhu, Y. L.; Ma, X. L.; Borisevich, A. Y.; Morozovska, A. N.; Eliseev, E. A.; Wang, W. Y.; Wang, Y. J.; Xu, Y. B.; Zhang, Z. D.; Pennycook, S. J. Observation of Aperiodic Array of Flux-Closure Quadrants in Strained Ferroelectric $PbTiO_3$ Films. *Science* **2015**, *348*, 547−551.

(3) Yadav, A. K.; Nelson, C. T.; Hsu, S. L.; Hong, Z.; Clarkson, J. D.; Schlepütz, C. M.; Damodaran, A. R.; Shafer, P.; Arenholz, E.; Dedon, L. R.; Chen, D.; Vishwanath, A.; Minor, A. M.; Chen, L. Q.; Scott, J. F.; Martin, L. W.; Ramesh, R. Observation of Polar Vortices in Oxide Superlattices. *Nature* **2016**, *530*, 198.

(4) Zheng, Y.; Chen, W. J. Characteristics and Controllability of Vortices in Ferromagnetics, Ferroelectrics, and Multiferroics. *Rep. Prog. Phys.* **2017**, *80*, No. 086501.

(5) Das, S.; Tang, Y. L.; Hong, Z.; Gonçalves, M. A. P.; McCarter, M. R.; Klewe, C.; Nguyen, K. X.; Gómez-Ortiz, F.; Shafer, P.; Arenholz, E.; Stoica, V. A.; Hsu, S.-L.; Wang, B.; Ophus, C.; Liu, J. F.; Nelson, C. T.; Saremi, S.; Prasad, B.; Mei, A. B.; Schlom, D. G.; Íñiguez, J.; García-Fernández, P.; Muller, D. A.; Chen, L. Q.;

Junquera, J.; Martin, L. W.; et al. Observation of Room-Temperature Polar Skyrmions. *Nature* **2019**, *568*, 368−372.
(6) Kim, J.; You, M.; Kim, K.-E.; Chu, K.; Yang, Ch.-H. Artificial Creation and Separation of a Single Vortex-Antivortex Pair in a Ferroelectric Flatland. *npj Quantum Mater.* **2019**, *4*, No. 29.
(7) Ding, L. L.; Ji, Y.; Zhang, X. Y.; Xiong, W. M.; Chen, W. J.; Zhang, B. M.; Wang, B.; Zheng, Y. Characterization and Control of Vortex and Antivortex Domain Defects in Quadrilateral Ferroelectric Nanodots. *Phys. Rev. Mater.* **2019**, *3*, No. 104417.
(8) Li, Z.; Wang, Y. J.; Tian, G.; Li, P. L.; Zhao, L. N.; Zhang, F. Y.; Yao, J. X.; Fan, H.; Song, X.; Chen, D. Y.; Fan, Z.; Qin, M. H.; Zeng, M.; Zhang, Z.; Lu, X. B.; Hu, S.; Lei, C.; Zhu, Q. F.; Li, J. Y.; Gao, X. S.; Liu, J.-M. High-Density Array of Ferroelectric Nanodots with Robust and Reversibly Switchable Topological Domain States. *Sci. Adv.* **2017**, *3*, No. e1700919.
(9) Tian, G.; Yang, W. D.; Song, X.; Zheng, D. F.; Zhang, L. Y.; Chen, C.; Li, P. L.; Fan, H.; Yao, J. X.; Chen, D. Y.; Fan, Zh.; Hou, Z.; Zhang, Z.; Wu, S. J.; Zeng, M.; Gao, X. S.; Liu, J.-M. Manipulation of Conductive Domain Walls in Confined Ferroelectric Nanoislands. *Adv. Funct. Mater.* **2019**, *29*, No. 1807276.
(10) Prosandeev, S.; Ponomareva, I.; Kornev, I.; Bellaiche, L. Control of Vortices by Homogeneous Fields in Asymmetric Ferroelectric and Ferromagnetic Rings. *Phys. Rev. Lett.* **2008**, *100*, No. 047201.
(11) Li, Ch.; Cao, Y. Y.; Bai, Y. H.; Li, A. D.; Zhang, S.; Wu, D. Electromechanical Response from $LaAlO_3/SrTiO_3$ Heterostructures. *ACS Appl. Mater. Interfaces* **2015**, *7*, 10146−10151.
(12) Tian, G.; Chen, D. Y.; Fan, H.; Li, P. L.; Fan, Zh.; Qin, M. H.; Zeng, M.; Dai, J. Y.; Gao, X. S.; Liu, J.-M. Observation of Exotic Domain Structures in Ferroelectric Nanodot Arrays Fabricated via a Universal Nanopatterning Approach. *ACS Appl. Mater. Interfaces* **2017**, *9*, 37219−37226.
(13) Park, S. M.; Wang, B.; Das, S.; Chae, S. Ch.; Chung, J.-S.; Yoon, J.-G.; Chen, L.-Q.; Yang, S. M.; Noh, T. W. Selective Control of Multiple Ferroelectric Switching Pathways using a Trailing Flexoelectric Field. *Nat. Nanotechnol.* **2018**, *13*, 366−370.
(14) Chen, P.; Zhong, X. L.; Zorn, J. A.; Li, M. Q.; Sun, Y. W.; Abid, A. Y.; Ren, C.; Li, Y. H.; Li, X. M.; Ma, X. M.; Wang, J. B.; Liu, K. H.; Xu, Z.; Tan, C. B.; Chen, L. Q.; Gao, P.; Bai, X. D. Atomic Imaging of Mechanically Induced Topological Transition of Ferroelectric Vortices. *Nat. Commun.* **2020**, *11*, No. 1840.
(15) Chen, W. J.; Zheng, Y.; Wang, B. Vortex Domain Structure in Ferroelectric Nanoplatelets and Control of its Transformation by Mechanical Load. *Sci. Rep.* **2012**, *2*, No. 796.
(16) Chen, W. J.; Zheng, Y. Vortex Switching in Ferroelectric Nanodots and its Feasibility by a Homogeneous Electric Field: Effects of Substrate, Dislocations and Local Clamping Force. *Acta Mater.* **2015**, *88*, 41−54.
(17) Balke, N.; Winchester, B.; Ren, W.; Chu, Y. H.; Morozovska, A. N.; Eliseev, E. A.; Huijben, M.; Vasudevan, R. K.; Maksymovych, P.; Britson, J.; Jesse, S.; Kornev, I.; Ramesh, R.; Bellaiche, L.; Chen, L. Q.; Kalinin, S. V. Enhanced Electric Conductivity at Ferroelectric Vortex Cores in $BiFeO_3$. *Nat. Phys.* **2012**, *8*, 81−88.
(18) Ruff, E.; Krohns, S.; Lilienblum, M.; Meier, D.; Fiebig, M.; Lunkenheimer, P.; Loid, A. Conductivity Contrast and Tunneling Charge Transport in the Vortexlike Ferroelectric Domain Patterns of Multiferroic Hexagonal $YMnO_3$. *Phys. Rev. Lett.* **2017**, *118*, No. 036803.
(19) Yadav, A. K.; Nguyen, K. X.; Hong, Z. J.; García-Fernández, P.; Aguado-Puente, P.; Nelson, C.; Das, S.; Prasad, B.; Kwon, D.; Cheema, S.; Khan, A. I.; Hu, C.; Íñiguez, J.; Junquera, J.; Chen, L.-Q.; Muller, D. A.; Ramesh, R.; Salahuddin, S. Spatially Resolved Steady-State Negative Capacitance. *Nature* **2019**, *565*, 468.
(20) Zubko, P.; Wojdel, J. C.; Hadjimichael, M.; Fernandez-Pena, S.; Sené, A.; Luk'yanchuk, I.; Triscone, J.-M.; Íñiguez, J. Negative Capacitance in Multidomain Ferroelectric Superlattices. *Nature* **2016**, *534*, 524.
(21) Ma, J.; Ma, J.; Zhang, Q. H.; Peng, R. C.; Wang, J.; Liu, Ch.; Wang, M.; Li, N.; Chen, M. F.; Cheng, X. X.; Gao, P.; Gu, L.; Chen, L.-Q.; Yu, P.; Zhang, J. X.; Nan, C.-W. Controllable Conductive Readout in Self-assembled, Topologically Confined Ferroelectric Domain Walls. *Nat. Nanotechnol.* **2018**, *13*, 947−952.
(22) Peng, R.-C.; Cheng, X. X.; Ma, J.; Huang, H. B.; Ma, J.; Chen, L.-Q.; Nan, C.-W. Understanding and Predicting Geometrical Constraint Ferroelectric Chargeddomain Walls in a $BiFeO_3$ Island via Phase-Field Simulations. *Appl. Phys. Lett.* **2018**, *113*, No. 222902.
(23) Chen, M. F.; Ma, J.; Peng, R.-C.; Zhang, Q. H.; Wang, J.; Liang, Y. H.; Wu, J. L.; Chen, L.-Q.; Ma, J.; Nan, C.-W. Robust Polarization Switching in Self-Assembled $BiFeO_3$ Nanoislands with Quad-Domain Structures. *Acta Mater.* **2019**, *175*, 324−330.
(24) Ma, J.; Wang, J.; Chen, M. F.; Peng, R.-C.; Ma, J.; Zhang, J. X.; Nan, C.-W. Geometry Confined Polar Vertex Domains in Self-assembled $BiFeO_3$ Nano-islands. *Mater. Res. Lett.* **2019**, *7*, 399−404.
(25) Kim, K.-E.; Jeong, S.; Chu, K.; Lee, J. H.; Kim, G.-Y.; Xue, F.; Koo, T. Y.; Chen, L.-Q.; Choi, S.-Y.; Ramesh, R.; Yang, C.-H. Configurable Topological Textures in Strain Graded Ferroelectric Nanoplates. *Nat. Commun.* **2018**, *9*, No. 403.
(26) Kim, K.-E.; Kim, Y.-J.; Zhang, Y.; Fei, X.; Kim, G.-Y.; Song, K.; Choi, S.-Y.; Liu, J.-M.; Chen, L.-Q.; Yang, C. H. Ferroelastically Protected Polarization Switching Pathways to Control Electrical Conductivity in Strain-graded Ferroelectric Nanoplates. *Phys. Rev. Mater.* **2018**, *2*, No. 084412.
(27) Xue, F.; Gu, Y.; Liang, L.; Wang, Y.; Chen, L.-Q. Orientations of Low-Energy Domain Walls in Perovskites with Oxygen Octahedral Tiles. *Phys. Rev. B* **2018**, *90*, No. 220101(R).
(28) Zhao, L. N.; Lu, Z. X.; Zhang, F. Y.; Tian, G.; Song, X.; Li, ZhW.; Huang, K. R.; Zhang, Zh.; Qin, M. H.; Wu, S. J.; Lu, X. B.; Zeng, M.; Gao, X. S.; Dai, J. Y.; Liu, J.-M. Current Rectifying and Resistive Switching in High Density $BiFeO_3$ Nanocapacitor Arrays on Nb-$SrTiO_3$ Substrates. *Sci. Rep.* **2015**, *5*, No. 9680.
(29) Fan, Z.; Yao, K.; Wang, J. Photovoltaic Effect in An Indium-Tin-Oxide/ZnO/$BiFeO_3$/Pt Heterostructure. *Appl. Phys. Lett.* **2014**, *105*, No. 162903.
(30) Chu, K.; Yang, C.-H. High-Resolution Angle-Resolved Lateral Piezoresponse Force Microscopy: Visualization of in-plane Piezoresponse vectors. *Rev. Sci. Instrum.* **2018**, *89*, No. 123704.

https://dx.doi.org/10.1021/acsami.0c19652
ACS Appl. Mater. Interfaces 2021, 13, 12331−12340